Supplemental Material for: Quantum interferometry with a g-factor-tunable spin qubit

K. Ono[1,2], S. N. Shevchenko[3,4,5], T. Mori[6], S. Moriyama[7], Franco Nori[3,8]

[1] *Advanced device laboratory, RIKEN, Wako-shi, Saitama 351-0198, Japan*

[2] *CEMS, RIKEN, Wako-shi, Saitama 351-0198, Japan*

[3] *Theoretical Quantum Physics Laboratory, RIKEN Cluster for Pioneering Research, Wako-shi, Saitama 351-0198, Japan*

[4] *B. Verkin Institute for Low Temperature Physics and Engineering, Kharkov 61103, Ukraine*

[5] *V. N. Karazin Kharkov National University, Kharkov 61022, Ukraine*

[6] *Nanoelectronics Research Institute, National Institute of Advanced Industrial Science and Technology (AIST), Tsukuba, Ibaraki 305-8568, Japan*

[7] *International Center for Materials Nanoarchitectonics, National Institute for Materials Science (NIMS), Tsukuba, Ibaraki 305-0044, Japan and*

[8] *Department of Physics, The University of Michigan, Ann Arbor, MI 48109-1040, USA*

(Dated: April 12, 2019)

In this Supplemental Material we present details about both our experimental layout and our theoretical approach. Also we provide here additional data for interferograms with various modulating signals.

I. DEVICE DETAILS

A. Tunnel field-effect transistor

The tunnel field-effect transistor (TFET) is a kind of metal-oxide-semiconductor field-effect transistor (MOSFET) that has an n-type source and a p-type drain electrodes, effectively working as a gated PIN diode (a diode with an undoped intrinsic semiconductor region between a p-type semiconductor and an n-type semiconductor region). Its channel, kept intrinsic for zero gate voltage V_G, can be tuned into p-(n-) type for large enough positive (negative) V_G. A TFET is tuned on by gate-induced reduction of the PIN junction thickness, enabling steeper switchings than MOSFET. Recently, it has been intensively studied as a future low-power transistor element for large-scale integration [1]. Enhancement of the on-current is achieved by introducing deep impurities in the (relatively long-channel) TFETs, and this enhancement is ascribed to deep-level assisted resonant tunneling in the PIN junction.

In order to electrically access a single deep impurity, and use its spin for a high-temperature qubit, we introduce deep impurities in a short-channel TFET. Tunneling transport through a deep impurity level as well as the gate tuning of the level are possible in short-channel TFET provided that the deep impurity is located appropriately in the channel. In contrast to a MOSFET, the impurity-electrode tunnel coupling can be in a reasonable range of the TFET for realistic channel lengths (several tens of nm), even when the deepest level is located in the middle of the band gap.

Our TFET-based devices are fabricated with a process compatible with those for standard MOSFETs. Starting from silicon-on-insulator wafers, n-type electrodes (followed by p-type electrodes) are defined by standard ion implantations of shallow donors (shallow acceptors). Then, we lay both Al and N by the ion implantations in the whole area including source, channel, and drain, and follow by appropriate heat treatment. This process is known to form coupled Al-N impurity pairs in Si [2–5]. We found this is crucial for introducing deep impurity levels to TFETs. Indeed, if we omit this process, no TFETs (including short-channel ones) show the quantum-dot-like transport as described below, but only conventional characteristics of TFETs. Finally, the gate electrodes are formed with standard high-k/metal gate technology.

Some of our devices show characteristics similar to a double dot, which is formed when two quantum dots are connected in series between source/drain electrodes. Measurements of Coulomb diamonds, Coulomb conductance peaks, and their temperature dependence suggest the formation of multiple dots in the device, composed of a deep impurity with strong confinement ($>$ 0.1 eV, a Al-N deep level) and at least one satellite dot nearby the deep impurity with weaker confinement ($\sim$ 5-10 meV), which is probably a shallow acceptor located close to the p-type drain electrode. Thus, interdot level detuning and interdot tunnel coupling are not tunable but nearly fixed. However, there is a little tunability for the tunnel coupling between the dots and the electrodes (leads). Because the space charge layer of the PIN structure depends on the V_{SD}, i.e. thicker for negative V_{SD} and vice versa. The tunnel coupling between the double dots and electrodes is smaller for negative V_{SD} (and vice versa).

We have checked the electron spin resonance (ESR) response of I_{SD} for various sets of (V_{SD}, V_G) in the range of 5-10 mV, and identified the spin blockade region in the plane of (V_{SD}, V_G). For the device used in the main text, we observed the ESR spectra with two resonant lines with g-factors equal to 2.3 and 2.7. The peak of the ESR with the g-factor 2.7 is weak.

B. High-temperature spin qubit

In Fig. 1 we present the schematic of the single-electron tunneling cycle in the spin-blockade regime. This is the same scheme as Fig. 1(c) in the main text. Here we describe this in more detail.

Consider the initial situation in (i) with one electron in the right dot. The localized energy level on the left (closer to the n-type source electrode) is the electron-number $N = 1$ state of the deep impurity, while the right two energy levels are those of the $N = 1$ and $N = 2$ states (separated by the on-site Coulomb energy $E_{\mathrm{C}} \sim 10$ meV) of the shallow impurity, respectively. The Fermi energy of the p-type electrode sits between the two right states with a thermal broadening $k_{\mathrm{B}}T$. The tunneling cycle occurs following the dark gray arrows, with equal probabilities for the (i)→(ii) and (i)→(ii') trajectories, and eventually is blocked at the parallel-spin state (ii'). Under the ESR condition of the right spin, the spin blockade is lifted, as shown in the inset, and the source-drain current is increased due to the newly opened cycle, as indicated with the light gray arrows: (i)→(ii')→(iii')→(iii)→(i). Note that the spin qubit energy levels have the separation $\Delta E \sim 9$ GHz$\cdot h$ at $B \sim 1$ T and the qubit transition is described as flipping of the spin at (ii')→(iii').

In the spin blockade condition in our experiment, the energy levels of each dot are placed at a position that is not affected by the thermally excited Fermi distribution of the source/drain electrodes. Under these circumstances, spins of the double dot are initialized to ↑↑ (up and up) or ↓↓ (down and down). Here we drive the spin state to ↑↓ or ↓↑ by irradiating with a microwave π pulse corresponding to one of the target spins (e.g., the second spin). This state is hybridized with the spin-triplet state (↑↓ + ↓↑), thus lifting the spin blockade, then one electron is emitted to the drain electrode, and another electron is reloaded to the double dot, and again initialized to ↑↑ or ↓↓. Thus, the increase of I_{SD} is a time-ensemble measure of the flipping rate of the target spin, from its initialized ↑ or ↓ state to the other state. In the calculation, we treat one 1/2-spin and it is always initialized to the ground state ↓, and the occupation of the upper level ↑ is calculated.

The coherence time T_2^* of the spin is estimated to be $\sim$ 0.2-0.3 μs from Rabi oscillations [6], which is consistent with the ESR line width of 4 MHz. The relaxation time T_1 cannot be estimated from our spin blockade detection scheme. At least we know that T_1 does not dominate the refreshment of the spin blockade and thus it is much longer than T_2^*.

In our previous work [6], the back plate was not grounded at the right hand side of Fig. 1(a). Thus, the AC electric field, rather than the AC magnetic field was applied to the impurity. So we concluded that the spin resonance observed in Ref. [6] was an electric dipole spin resonance, rather than an electron spin resonance. In this work, we have improved this point and an AC magnetic field is applied, rather than an AC electric field.

C. Tuning the g-factor by the gate voltage

We have implanted Al-N coupled impurity pairs as the deep impurity. A large anisotropy of its g-factor (2.0-2.3 depending on the magnetic field direction) has been reported in Ref. [6]. The anisotropy of the g-factor of Al-N centers has also been reported for bound excitons trapped to the Al-N center [2]. These results suggest that the wave function of the Al-N center is strongly localized and has axial symmetry, and its spin-orbit interaction is strong and anisotropic. In such system, the g-factor should also react with an electric field which modifies its wave function, and results in the observed gate-voltage dependence of the g-factor. However, the detailed nature of the deep impurity is unknown and its identification is a future research subject.

Changing the gate voltage V_G within the spin-blockade region changes the g-factor by about 1% [6]. In such system the g-factor should also react with an electric field which modifies its wave function (Stark effect), and results in the observed gate-voltage dependence of the g-factor.

Figure 2(a) shows the ESR peak observed in the spin-blockade regime. The ESR linewidth, i.e., the inverse of the coherence time T_2^*, is reasonably limited by the spin blockade lifetime as well as the natural abundance of ^{29}Si [7]. Changing the gate voltage V_G within the spin blockade region changes the g-factor by about 1% due to the Stark effect [Fig. 2(b)] [8]. Therefore, the device behaves as a spin qubit.

Two ESR transitions with g-factors $g = 2.3$ and $g = 2.7$ for the two impurities are observed. Hereafter, we only focus on the ESR peaks at $g = 2.3$.

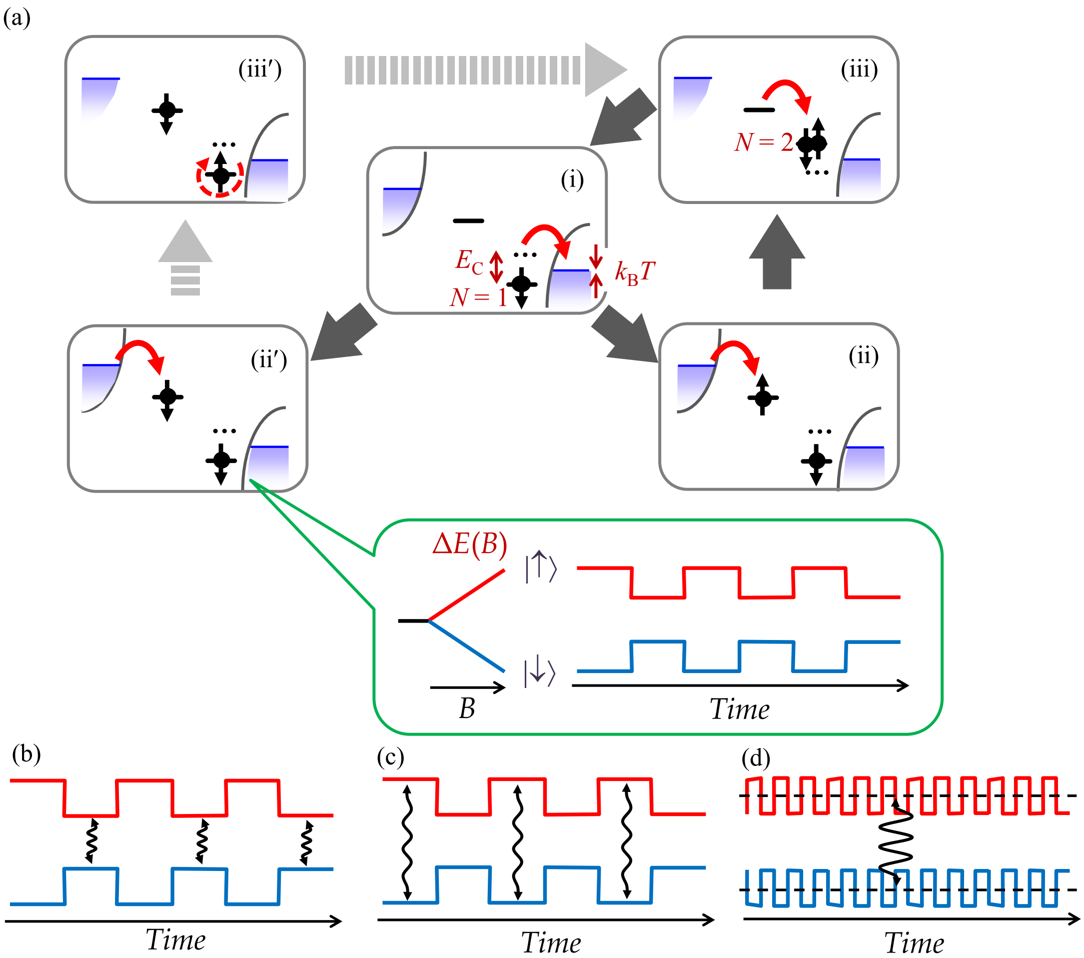

FIG. 1: **Schematics of the g-factor modulation and ESR.** (a) The Zeeman energy of the spin is modulated in time by a square waveform. Note that the spin blockade condition is always kept under modulation. (b) Schematic of the ESR for the slow limit of the square-wave modulation, where the low-energy spin state is hit by a low ESR microwave frequency. (c) The same slow-modulation limit, where the high-energy spin state is resonant with the high-frequency ESR microwave. (d) High modulation-frequency limit, where the spin energy is motional-averaged and the ESR occurs for an averaged microwave frequency.

II. THEORETICAL DESCRIPTION OF THE DRIVEN AND MODULATED SINGLE SPIN

A. Energy-level modulations

Consider a two-level system, described by the Hamiltonian

$$H(t) = \frac{B_z(t)}{2}\sigma_z + \frac{B_x(t)}{2}\sigma_x \tag{1}$$

with

$$B_z(t)/\hbar = \omega_0 + \delta \cdot s(t), \tag{2}$$

where we assume the amplitude to be small, i.e. $\delta \ll \omega_0$, and

$$B_x(t)/\hbar = 2G\cos\omega t. \tag{3}$$

(Here the factor 2 is introduced so that the amplitude G defines the Rabi frequency.)

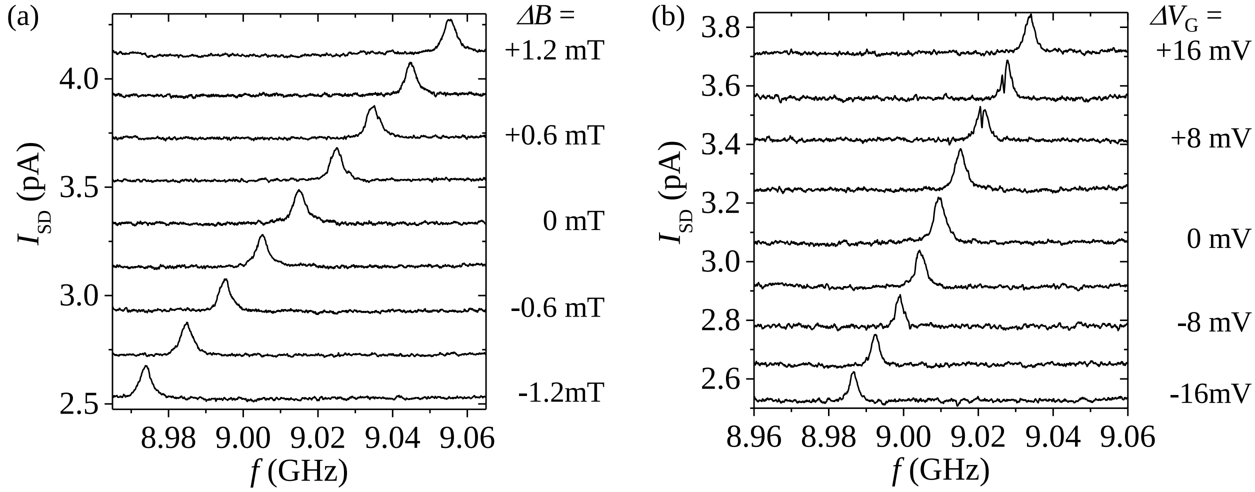

FIG. 2: **ESR for the single-spin qubit with tunable g-factor.** (a) The source-drain current I_{SD} of the device at V_{SD} = 0.33 V and $V_G = -0.36$ V as a function of the frequency f for various magnetic field detunings ΔB from $B = 0.2755$ T, with fixed MW power of -18 dBm. ESR peaks with a linewidth of 4 MHz are observed. (b) I_{SD} of the device at $V_{SD} = 0.33$ V and $B = 0.2755$ T versus the frequency f for various gate voltage detuning ΔV_G away from $V_G = -0.36$ V. The g-factor (thus the qubit energy) is increased for more positive ΔV_G. The change of the g-factor is found to be linearly dependent on ΔV_G. For $|\Delta V_G| > 20$ mV, the ESR response is not observed, suggesting the V_G is out of the SB region. Note that the ESR peak is superimposed on the background current, which is around 2.5 pA. Both in (a) and (b) all the upper curves are shifted vertically, for clarity.

For the longitudinal-field modulation, we consider different possibilities: (i) sinusoidal modulation, (ii) asymmetric latching modulation, and (iii) ramp modulation. Below we will discuss these regimes in more detail.

(i) The sinusoidal modulation is the one most often used, and it is given by

$$s^{(i)}(t) = \cos \Omega t = \cos 2\pi\tau, \tag{4}$$

where we introduced the dimensionless time

$$\tau = \frac{\Omega t}{2\pi}. \tag{5}$$

(ii) Next we consider a modulation with asymmetric rectangular pulses with duty ratio d. This corresponds to a qubit latched in one of the two states, with fast switching between these states. We refer to this regime as “latching modulation” [9]. In this case we assume that the modulating function has two stages with equal areas under the curve:

$$s_d^{(ii)}(\tau) = \begin{cases} 2d, & 0 < \tau < 1-d, \\ -2\,(1-d)\,, & 1-d < \tau < 1. \end{cases} \tag{6}$$

Here the factor 2 is introduced so that this modulating function changes between -1 and $+1$ for the symmetric 50% duty ratio:

$$s_{0.5}^{(ii)}(\tau) = \begin{cases} 1, & 0 < \tau < 0.5, \\ -1, & 0.5 < \tau < 1. \end{cases} \tag{7}$$

These two definitions can be written (with an insignificant shift of the time variable) as

$$s_d^{(ii)}(\tau) = 2\theta\,(\cos 2\pi\tau + \cos \pi d) - 2\,(1-d) \tag{8}$$

and

$$s_{0.5}^{(ii)}(\tau) = \mathrm{sgn}\,(\cos 2\pi\tau)\,, \tag{9}$$

where sgn is the sign function.

(iii) Modulating with triangular pulses, or "ramp modulation", corresponds to

$$s^{(iii)}(\tau) = \{\tau\}, \tag{10}$$

where the curly brackets denote the fractional part.

In all cases the modulation frequency is assumed to be small,

$$\Omega \ll \omega. \tag{11}$$

For this reason, the fast signal with frequency ω can be called "driving", while the slow signal with frequency Ω can be denoted as the "energy-level modulation".

B. Bloch equations and the rotating-wave approximation

With the Hamiltonian (1) the qubit dynamics can be described by the Bloch equations (as e.g. in Ref. [10]) for the components of the density matrix $\rho = \frac{1}{2}(1 + X\sigma_x + Y\sigma_y + Z\sigma_z)$:

$$\begin{cases} \dot{X} = -B_z Y - \Gamma_2 X, \\ \dot{Y} = -B_x Z + B_z X - \Gamma_2 Y, \\ \dot{Z} = B_x Y - \Gamma_1 (Z - Z_0). \end{cases} \tag{12}$$

Here the phenomenological parameters $\Gamma_1 = T_1^{-1}$ and $\Gamma_2 = T_2^{-1}$ are the relaxation rates with decoherence rate $\Gamma_2 = \frac{1}{2}\Gamma_1 + \Gamma_\phi$, defined by the pure dephasing rate Γ_ϕ. Decoherence defines the relaxation of X and Y towards 0, while the relaxation of the diagonal component Z is defined by the Maxwell-Boltzmann distribution for the given effective temperature T_{eff}, and it evolves towards $Z_0 = \tanh[\hbar\omega_0/(2k_B T_{\text{eff}})]$.

It is often instructive to solve the Bloch equations analytically. There are several approaches, such as the adiabatic-impulse model and the rotating-wave approximation (RWA). We refer the interested reader to Refs. [9, 11] and references therein for the adiabatic-impulse and other models, while the RWA calculations are presented below in detail.

Based on the slowness of the energy-level modulation, Eq. (11), we can make use of the RWA, following Refs. [9] and [11]. First, we make the unitary transformation

$$U_1 = \exp(-i\omega\sigma_z t/2), \tag{13}$$

which corresponds to moving to the rotating frame, to get rid of the fast time dependence. In the new representation, the Hamiltonian reads

$$H_1 = U_1^\dagger H U_1 - i\hbar U_1^\dagger \dot{U}_1 = \frac{\hbar}{2}[\Delta\omega + f(t)]\sigma_z + \frac{\hbar G}{2}\sigma_x, \tag{14}$$

where $f(t) = \delta \cdot s(t)$ and $\Delta\omega = \omega_0 - \omega$. Next, in order to have the Hamiltonian conveniently written to solve the Bloch equations, we make another unitary transformation,

$$U_2 = \exp[-i\eta(t)\sigma_z/2], \qquad \eta(t) = \int_0^t dt' f(t'). \tag{15}$$

We obtain a new Hamiltonian

$$H_2 = \frac{\hbar\Delta\omega}{2}\sigma_z + \frac{\hbar}{2}G\left(e^{i\eta}\sigma_+ + h.c.\right), \tag{16}$$

with $\sigma_+ = \frac{1}{2}(\sigma_x + i\sigma_y)$. Then the preparatory stage is finalized by the Fourier-series expansion,

$$e^{i\eta} = \sum_{m=-\infty}^{\infty} \Delta_m e^{im\Omega t}, \tag{17}$$

where the complex-valued amplitude is given by the inverse Fourier transform,

$$\Delta_m = \frac{\Omega}{2\pi}\int_0^{2\pi/\Omega} dt e^{-im\Omega t} e^{i\eta(t)} = \int_0^1 d\tau \exp[i\eta(\tau) - i2\pi m\tau]. \tag{18}$$

Then the Hamiltonian becomes

$$H_2 = \frac{\hbar\Delta\omega}{2}\sigma_z + \frac{\hbar G}{2}\sum_{m=-\infty}^{\infty}\left(\Delta_m e^{im\Omega t}\sigma_+ + h.c.\right). \tag{19}$$

To solve the Bloch equations, for the moment we assume that the system is driven close to resonance, where the "dressed energy distance" $\hbar\Delta\omega$ equals to the energy of k photons, $\hbar\Delta\omega \approx k\hbar\Omega$. Then we omit the "fast-rotating" terms and leave only terms with $m = k$. With this, the r.h.s. of the Bloch equations does not contain any explicit time dependence. Then equating its l.h.s. to zero, we obtain the stationary solution. In particular, this gives the upper-level occupation probability, $P_+ = \frac{1}{2}(1 - Z)$. Summing all possible resonant terms, we obtain the qubit upper-level occupation probability

$$P_+\left(\Delta\omega, \frac{\delta}{\Omega}\right) = \frac{1}{2}\sum_{k=-\infty}^{\infty}\frac{G_k^2(\delta/\Omega)}{G_k^2(\delta/\Omega) + \frac{\Gamma_1}{\Gamma_2}\left(\Delta\omega - k\Omega\right)^2 + \Gamma_1\Gamma_2}, \tag{20}$$

where $G_k(x) = G\left|\Delta_k(x)\right|$. We emphasize, that for a complex-valued Δ_k, what matters is its absolute value.

C. Calculations for different modulations

As shown in Eq. (20), in order to obtain the upper-level occupation probability, one has to calculate the functions Δ_k. This is the subject of the present subsection.

(i) For the sinusoidal modulation, we can make use of the Jacobi-Anger expansion, which reads

$$\exp\left(ix\sin 2\pi\tau\right) = \sum_{m=-\infty}^{\infty} J_m(x)\, e^{im2\pi\tau}, \tag{21}$$

where $J_m(x)$ is the Bessel function of the first kind. Then, it is straightforward to see that

$$\Delta_m^{(i)}(x) = J_m(x), \qquad x = \frac{\delta}{\Omega}. \tag{22}$$

It is useful to recall here the asymptote

$$J_m(x) \approx \sqrt{\frac{2}{\pi x}}\cos\left[x - \frac{\pi m}{2} - \frac{\pi}{4}\right]. \tag{23}$$

(ii) For the asymmetric latching modulation, by direct integration we obtain

$$\Delta_{d,m}^{(ii)}(x) = \frac{2}{\pi}\frac{x\sin\left[\pi\left(1-d\right)\left(m - 2dx\right)\right]}{\left(m + 2\left(1-d\right)x\right)\left(m - 2dx\right)}. \tag{24}$$

As mentioned before, since only $|\Delta_m|$ matters in Eq. (20), we omitted factors with unit modulus. We will do this throughout.

In particular, for the symmetric rectangular modulating signal with $d = 0.5$, Eq. (24) gives

$$\Delta_{0.5,m}^{(ii)}(x) = \frac{2}{\pi}\frac{x}{m^2 - x^2}\sin\left[\frac{\pi}{2}\left(m - x\right)\right]. \tag{25}$$

(iii) For the ramp modulation, we have

$$\Delta_m^{(iii)}(x) = \int_0^1 d\tau \exp\left[i\pi\left(x\tau^2 - 2m\tau\right)\right]. \tag{26}$$

This can be rewritten in terms of the Fresnel integrals:

$$\left|\Delta_m^{(iii)}(x)\right|^2 = \frac{1}{\pi x}\left[C\left(\sqrt{\pi x}\left(1-\frac{m}{x}\right)\right)+C\left(\sqrt{\pi x}\frac{m}{x}\right)\right]^2 + \\ +\frac{1}{\pi x}\left[S\left(\sqrt{\pi x}\left(1-\frac{m}{x}\right)\right)+S\left(\sqrt{\pi x}\frac{m}{x}\right)\right]^2, \tag{27}$$

$$S(y)=\int_0^y dt \sin t^2, \quad C(y)=\int_0^y dt \cos t^2. \tag{28}$$

Such rewriting allows to use asymptotic approximations. In particular, when $|y|\gg 1$

$$S(y)\approx C(y)\approx \sqrt{\frac{\pi}{8}}\,\mathrm{sgn}\, y, \tag{29}$$

which gives

$$\left|\Delta_m^{(iii)}(x)\right| \approx 1/\sqrt{x}. \tag{30}$$

The above equations allow to plot interferograms. We generated the right panels of Figs. 2-4 in the main text and the interferograms below (lower panels of Figs. 3 and 4 and the right panel of Fig. 6) employing Eq. (20). In addition, we used the Δ_k from Eqs. (22, 24, 25, and 26) for the sinusoidal, asymmetric and symmetric latching, and ramp modulations, respectively. For calculations, we took the parameters known from the experiment related to the driving and modulation as well as ω_0 and Γ_2, while the two unknown parameters, G and Γ_1, were used for fitting. We emphasize that the interference pictures are very sensitive to the relaxation and decoherence rate, so, having obtained the agreement between the experimental and theory interferograms, we can state that we have reliably obtained the relaxation and decoherence rates. Finally, we note that we have checked that the interferograms calculated analytically with these equations agree nicely with the ones calculated numerically by solving Eq. (12).

D. Limiting cases

Equation (20), together with the expression of $\Delta_k(x)$ [Eqs. (22-26)], allows for an analytical treatment. Let us consider several illustrative limiting cases.

First, let us consider the symmetric latching modulation, with $\Delta_k(x)$ given by Eq. (25). For low modulating frequencies, $\Omega \ll \delta$, we have $x=\delta/\Omega \gg 1$ and $|k|\gg 1$. As a result, from Eq. (25) we obtain that, for any given value of x, the contribution comes from the two k-th terms with $k\simeq \pm x$, for which we obtain $\Delta_k(x)\simeq 1/2$. Inserting this result in Eq. (20) we find that the position of the resonances are at $\Delta\omega = k\Omega$, which, for $k=\pm x$, gives two lines at

$$\Delta\omega = \pm\delta. \tag{31}$$

At large modulating frequencies, $\Omega \gg \delta$, we have $x \ll 1$ and $k=0$. This is because for non-zero k we have $\Delta_k \sim x/k^2 \longrightarrow 0$. As a consequence, the position of the resonance is defined by $\Delta\omega = k\Omega$, which, for the main peak, with $k=0$, gives a zero shift of the resonance line:

$$\Delta\omega = 0. \tag{32}$$

With $\Delta_k \simeq 1/2$, we can estimate the frequency half-width at half-maximum $\Delta\omega_{\mathrm{HWHM}}$ by equating $\frac{1}{2}P_+$ at $\Delta\omega = k\Omega$ and P_+ at $\Delta\omega = k\Omega + \Delta\omega_{\mathrm{HWHM}}$. This gives

$$\Delta\omega_{\mathrm{HWHM}}^2 = \Gamma_2^2 + \frac{G^2}{4}\frac{\Gamma_2}{\Gamma_1}. \tag{33}$$

This means that the minimal half-width is Γ_2 and it is increased by the driving amplitude G.

Even more informative is the asymmetric latching modulation, with $d \neq 1/2$. For low modulating frequencies, $x \ll 1$, there are two characteristic values of k, defined from the denominator of Eq. (24). For $k=2(1-d)x$, we have $\Delta_k \simeq d$ and $\Delta\omega = k\Omega$, so that

$$\Delta\omega = 2(1-d)\delta. \tag{34}$$

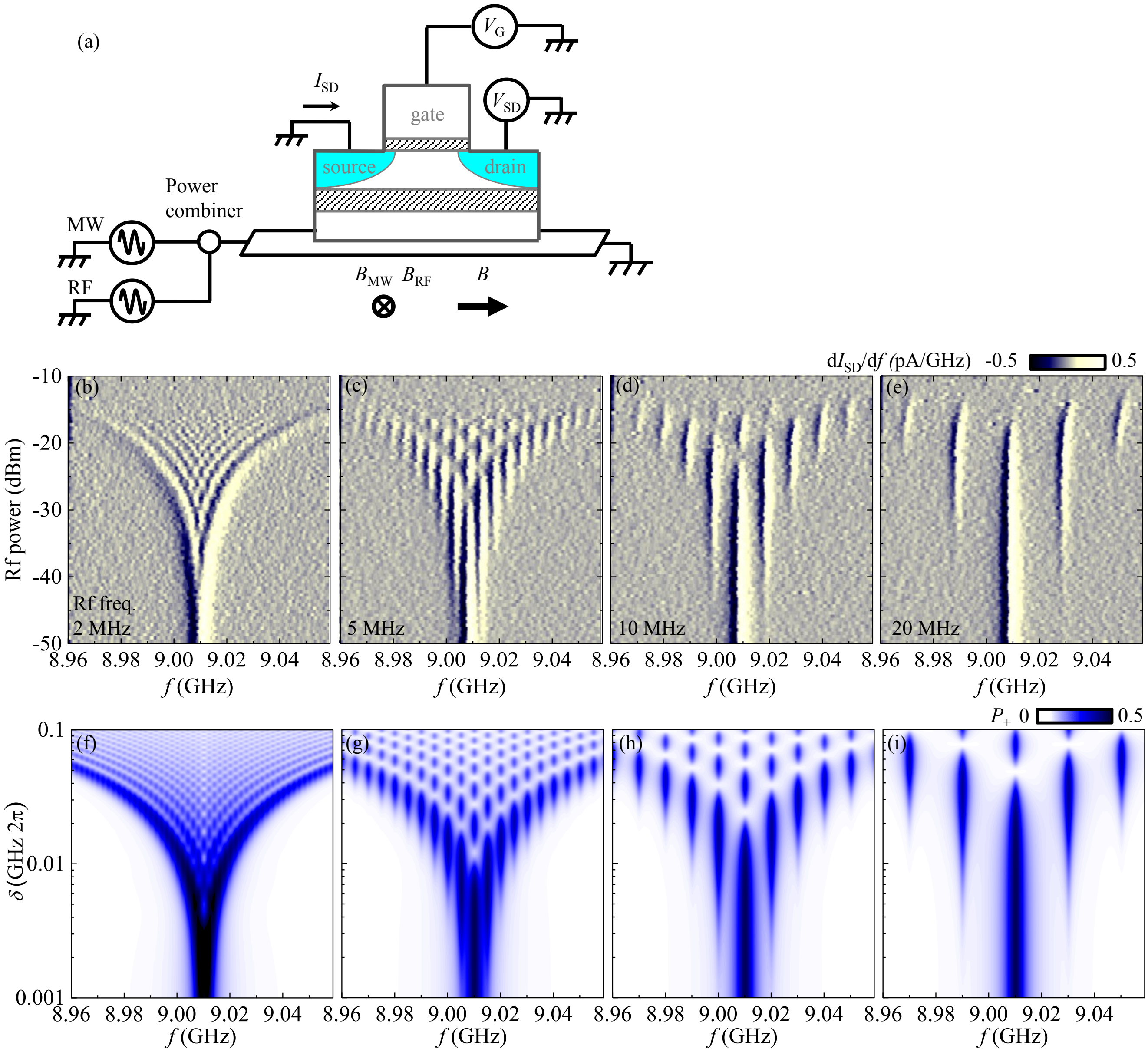

FIG. 3: Radio frequency (RF) wave power dependence of Landau-Zener-Stückelberg-Majorana (LZSM) interference of the spin resonance signal. (a) Schematic measurement set up. Instead of modulating the g-factor by V_G, here we add the rf signal to the microwave signal with the power combiner. This set up is effectively equivalent to the set up of Fig. 1(a) because the rf signal is fed to the gate via a stray capacitance between the substrate and the gate. (b-e) the RF power dependence of the LZSM interference with fixed RF frequency of (b) 2 MHz, (c) 5 MHz, (d) 10 MHz, and (e) 20 MHz, respectively. (f-i) shows the corresponding calculations. For calculations the following parameters were used for all the graphs: $G/2\pi = 1$ MHz, $\Gamma_1/2\pi = 0.2$ MHz, $\Gamma_2/2\pi = 1$ MHz.

For $k = -2dx$, we have $\Delta_k \simeq 1 - d$, and

$$\Delta\omega = -2d\delta. \tag{35}$$

We can see that the two terms, with different k, define the positive and negative shifts of different signs, Eqs. (34-35), which for $d = 1/2$ reduce to Eq. (31). From Eq. (20) we can also define the heights of the two respective peaks, at $\Delta\omega = k\Omega$ and for given values of k's we obtain

$$P_+^L = \frac{1}{2}\frac{d^2}{d^2 + \lambda}, \qquad P_+^H = \frac{1}{2}\frac{(1-d)^2}{(1-d)^2 + \lambda}, \qquad \lambda = \frac{\Gamma_1\Gamma_2}{G^2}. \tag{36}$$

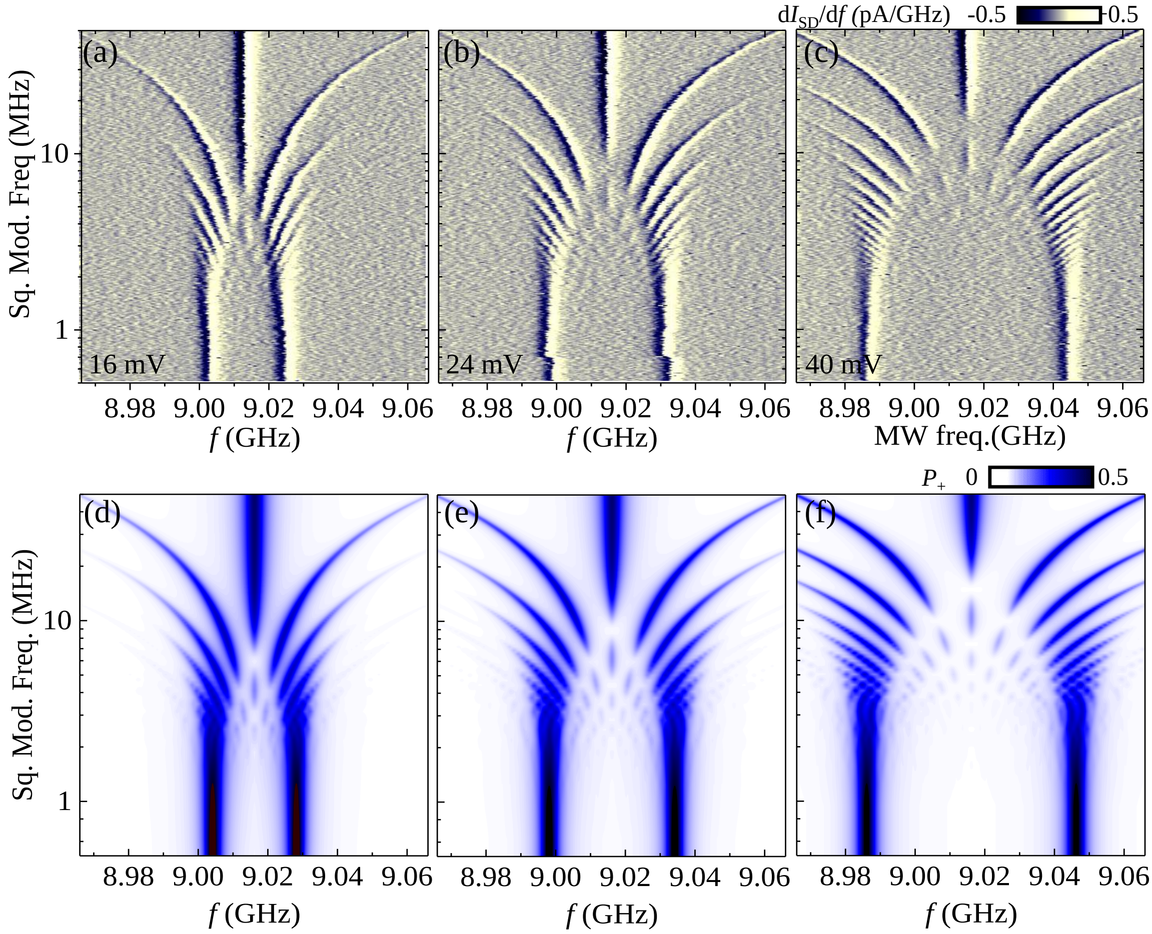

FIG. 4: Amplitude dependence of the square-wave modulation. (a-c) Similar measurements as Fig. 3(c) in the main text with different amplitudes of the square-wave modulation, (a) 16 mV, (b) 24 mV, and (c) 40mV, respectively. (d-f) shows the corresponding calculations, using $\delta/2\pi = 12$, 18, 30 MHz for (d)-(f), respectively.

In this way, the asymmetric latching is defined by the d-dependent peaks at small modulating frequency, while for the large modulating frequency we again have $\Delta\omega = k\Omega$ with $k = 0$, i.e. the zero frequency shift, as above in Eq. (32), which is remarkably independent of d.

From our formulas, we can also estimate the modulating frequency Ω, at which transition from one regime (high-frequency one, with the interference fringes) to another regime (low-frequency one, with two resonance lines described by Eq. (31)) takes place. For this, we can estimate from Eq. (20) both the width of the k-th resonance and the distance between neighboring resonances. Let us define the transition frequency Ω_* as the one at which those two values become equal. Then we obtain

$$\Omega_* = 2\sqrt{\Gamma_2^2 + G_k^2\frac{\Gamma_2}{\Gamma_1}} \gtrsim 2\Gamma_2. \tag{37}$$

When G is small, this gives $\Omega_* \approx 2\Gamma_2$. For our parameters, with $\Delta_k \simeq 1/2$, this gives $\Omega_*/2\pi \approx 3$ MHz, in agreement with what we can see in both the simulations and the experiment in Fig. 4.

E. Interferograms

As predicted by the formula (20), there are resonances (when the denominator has minima) and nodes (when the numerator tends to zero). The respective resonance lines interrupted by the nodes form interference fringes, containing important information about the system and its environment. [11] The overall upper-level occupation probability P_+ depends on both $\Delta\omega$ and δ/Ω. Thus, the fringes can be visualized by plotting the qubit upper-level occupation (in

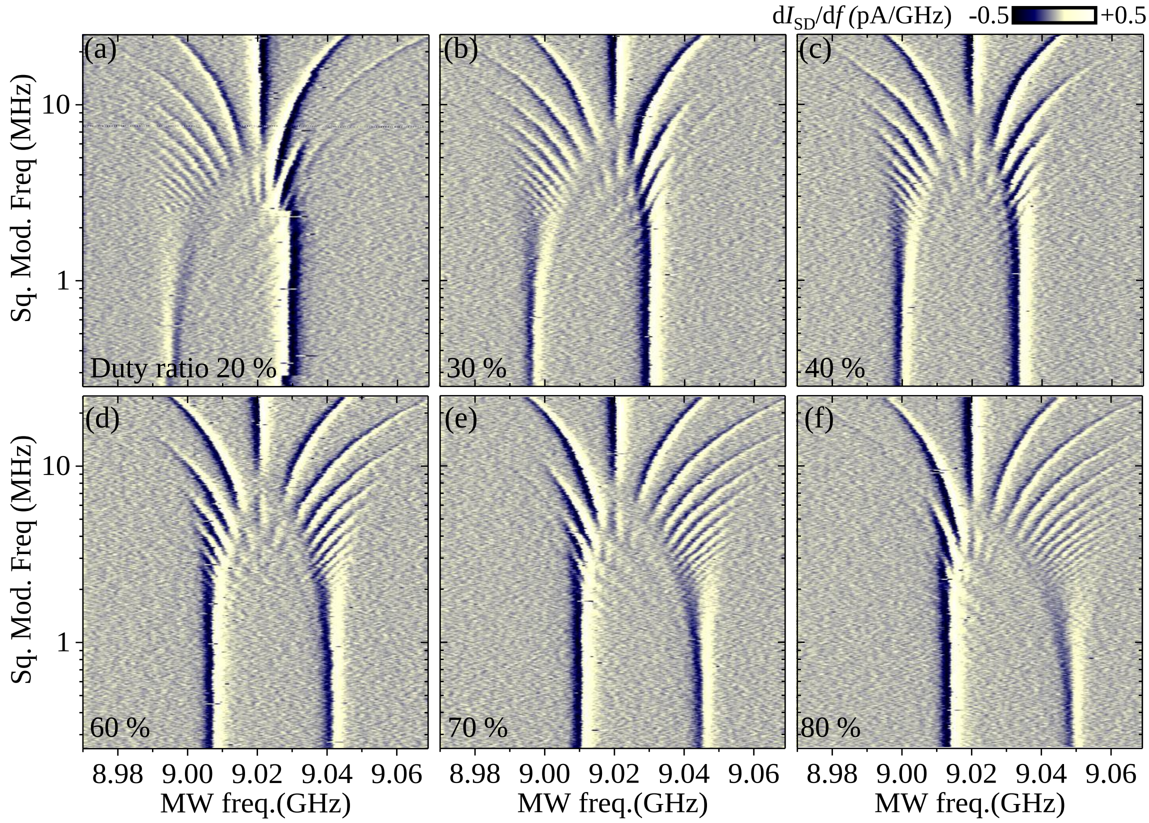

FIG. 5: Duty-ratio dependence of the asymmetric square-wave modulations. (a-f) Similar measurements as in Fig. 4(c) in the main text with different duty ratios of the asymmetric square-wave modulation, (a) 20%, (b) 30%, (c) 40%, (d) 60%, (e) 70%, and (f) 80%, respectively.

theory) or the source-drain current (in experiment) as a function of these parameters. One can choose either a pair $\Delta\omega$ and δ or $\Delta\omega$ and Ω. In the main text and in the Supplemental Material we mostly follow the latter option, while the dependence on the rf power (the former option) is presented below in Fig. 3.

There are two models which are convenient to understand and describe the interference: the so-called adiabatic-impulse model and the RWA. As presented in Refs. [9, 11], the two models give results. Here, for a qubit with various energy-level modulations, we used the RWA. Let us now summarize several key features of the two models.

If a two-level system is periodically driven, this can be described as an alternation of two processes: adiabatic evolution along the ground and excited qubit states most of the time, with sudden transitions between the two states, when they approach each other. The latter are known as Landau-Zener transitions, while the adiabatic evolution is described by the accumulation of the so-called Stückelberg phase. This phase produces the interference. Since related phenomena were also considered in 1932 by Majorana, the overall picture is related to four names: Landau, Zener, Stückelberg, and Majorana. Varying the system parameters, one can observe the alteration of the constructive and destructive interference.

While the adiabatic-impulse model could provide an intuitive picture, in our case (of rf-modulation plus mw-driving), it is more informative to use the RWA. This was considered in detail in this Section, and more graphical results will be presented in the next Section. As we mention after Eq. (4) in the main text, the dressed qubit is excited under the resonant condition, $\Delta\omega = k\Omega$. As can be seen from Eq. (20), the resonance lines are interrupted by zeros, when $\Delta_k(x) = 0$. Indeed, there we have destructive Stückelberg interference.

III. DETAILS OF EXPERIMENTAL AND CALCULATION RESULTS FOR THE MODULATED SINGLE SPIN

A. Sinusoidal modulation

The radio frequency (RF) wave power dependence of the Landau-Zener-Stückelberg-Majorana (LZSM) interference of the spin-resonance signal is summarized in Fig. 3. The intervals between the satellite peaks are defined by the RF frequencies, and the heights of the main and satellite peaks follow Bessel functions as a function of the RF power.

Note that a small and very slow drift of the ESR frequency ($\sim$ 20 MHz per week) is observed for fixed V_G that seems to depend on the filing condition of liquid helium of the cryostat, probably due to the small change of the position of the superconducting magnet. The effect of this slow drift is negligible during the 1 hour measurement, but induces variations of the ESR frequency f_0 at $V_G = -0.36$ V from 9.00 to 9.01 GHz.

B. Symmetric square-wave modulation

If the modulation is slow enough, then in the response there are two separate peaks situated at the two resonance frequencies corresponding to the two states. Increasing the modulation frequency, the coherent response is displayed as an averaged signal, situated at a frequency between the two resonance frequencies mentioned above, which is known as motional narrowing. One of the relevant time scales that sets the cross-over to motional averaging is the dynamical time scale associated with the difference in frequency of the two states that the system is modulated between. Another relevant time scale is the effective coherence time T_2^*. The smaller time of these is the characteristic time for the crossover. We note that the T_2^* of the qubit is limited not only by the nuclear spins but also by the lifetime (refresh time) of the spin blockade. Namely, the spin blocked state in the panel (ii') of Fig. 1(c) has a finite lifetime due to the higher-order tunneling pass that leads the state (ii') directly to the state (i).

The amplitude dependence of the square-wave modulation is shown in Fig. 4, which demonstrates that there are two characteristic frequencies. First, by increasing the modulating frequency, at $\Omega \approx \Omega_1 = 2 \cdot 2\pi$ MHz the transient behavior with interference fringes start to appear. Our calculations, demonstrate that this characteristic frequency is defined by the decoherence, $\Omega_1 = 2\Gamma_2$ and it is independent of the modulating amplitude δ. By further increasing the frequency, we can observe a kind of motional averaging, with one principal peak at $\Delta f = 0$ [12] replacing the two peaks at $f_{1,2} - f_0 = \pm\delta$. The appearance of this peak depends on the amplitude δ and is independent on the decoherence rate; this happens at $\Omega \approx \Omega_2 = \delta/2$ [12].

C. Asymmetric latching modulation

The duty ratio dependence of the asymmetric square-wave modulations is shown in Fig. 5. Data for Fig. 4(h) and (i) in the main text are extracted from these, as well as from Fig. 3(c) in the main text for the 50% duty ratio.

D. Ramp modulation

We have checked the effect of time reversal symmetry of the ramp waveform [Fig. 6(a)]. It is nearly identical to Fig. 5(c) in the main text. Figure 6(b) is the derivative, dP_+/df, of the Fig. 5(d) in the main text. Interference fringes with smaller wave length around the modulation frequency of 2 MHz are not clearly seen in the P_+ intensity plot [Fig. 5(d)]. For a more detailed study to check the time-reversal symmetry of the spin dynamics under a ramp modulation, it might be necessary to also reverse the magnetic field direction and microwave phase to properly implement the time-reversed process.

---

[1] A. M. Ionescu and H. Riel, "Tunnel field-effect transistors as energy-efficient electronic switches," Nature **479**, 329–337 (2011).

[2] J. Weber, W. Schmid, and R. Sauer, "Localized exciton bound to an isoelectronic trap in silicon," Phys. Rev. B **21**, 2401 (1980).

[3] R. Sauer, J. Weber, and W. Zulehner, "Nitrogen in silicon: Towards the identification of the 1.1223-eV (A, B, C) photoluminescence lines," Appl. Phys. Lett. **44**, 440–442 (1984).

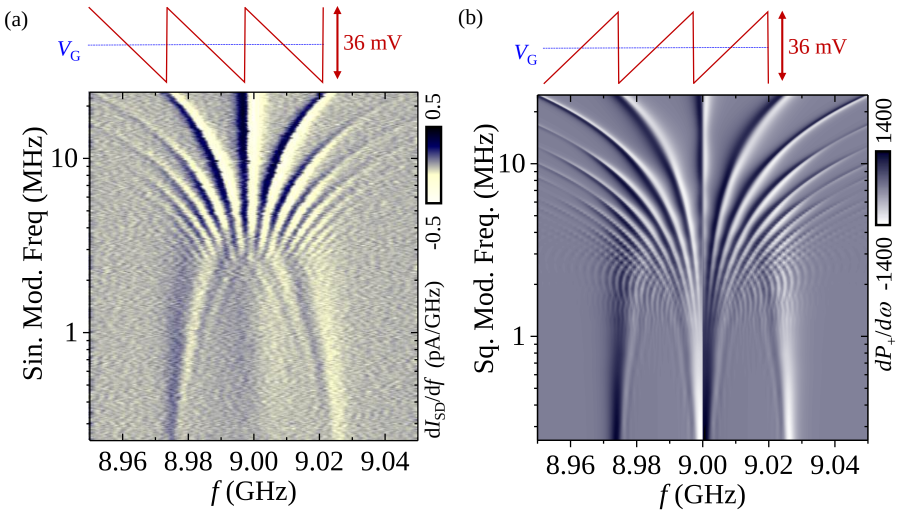

FIG. 6: Ramp modulations. (a) Measured ramp-modulation frequency dependence similar to Fig. 5(c) in the main text, but with inverted ramp waveform. (b) Intensity plot of the derivative dP_+/df. Data is the same as in Fig. 5(d) in the main text.

[4] R. A. Modavis and D. G. Hall, "Aluminum-nitrogen isoelectronic trap in silicon," J. Appl. Phys. **67**, 545–547 (1990).

[5] S. Iizuka and T. Nakayama, "First-principles calculation of electronic properties of isoelectronic impurity complexes in Si," Appl. Phys. Expr. **8**, 081301 (2015).

[6] K. Ono, T. Mori, and S. Moriyama, "High-temperature operation of a silicon qubit," Sci. Rep. **9**, 469 (2019).

[7] J. J. Pla, K. Y. Tan, J. P. Dehollain, W. H. Lim, J. J. L. Morton, D. N. Jamieson, A. S. Dzurak, and A. Morello, "A single-atom electron spin qubit in silicon," Nature **489**, 541–545 (2012).

[8] R. Rahman, S. H. Park, T. B. Boykin, G. Klimeck, S. Rogge, and L. C. L. Hollenberg, "Gate-induced g-factor control and dimensional transition for donors in multivalley semiconductors," Phys. Rev. B **80**, 155301 (2009).

[9] M. P. Silveri, K. S. Kumar, J. Tuorila, J. Li, A. Vepsäläinen, E. V. Thuneberg, and G. S. Paraoanu, "Stückelberg interference in a superconducting qubit under periodic latching modulation," New J. Phys. **17**, 043058 (2015).

[10] S. N. Shevchenko, A. S. Kiyko, A. N. Omelyanchouk, and W. Krech, "Dynamic behavior of Josephson-junction qubits: crossover between Rabi oscillations and Landau-Zener transitions," Low Temp. Phys. **31**, 569–576 (2005).

[11] S. N. Shevchenko, S. Ashhab, and F. Nori, "Landau-Zener-Stückelberg interferometry," Phys. Rep. **492**, 1–30 (2010).

[12] J. Li, M. P. Silveri, K. S. Kumar, J.-M. Pirkkalainen, A. Vepsäläinen, W. C. Chien, J. Tuorila, M. A. Sillanpää, P. J. Hakonen, E. V. Thuneberg, and G. S. Paraoanu, "Motional averaging in a superconducting qubit," Nat. Comm. **4**, 1420 (2013).